Multi-spatial-temporal-scale Coordinated Optimal Scheduling of Integrated Energy System Considering Frequency Support Ability

Yi Yang, Ping Tang, Can Wang, Nan Yang, Hui Ma, and Zhuoli Zhao

***Abstract*—Integrated energy system (IES) integrates various energy subsystems such as electricity, natural gas, heat, and the dynamic characteristics of different energy networks differ significantly. To realize the coordinated operation of heterogeneous energy flow network of electricity, natural gas, and heat, in this paper, a multi-spatial-temporal-scale coordinated optimal scheduling method of IES considering frequency support ability is presented. The method divides the IES into three layers on the spatial scale and divides IES optimal scheduling into three stages: day-ahead, intra-day and real-time on the temporal scale. In the day-ahead stage, the most economical day-ahead scheduling plan is developed. In the intra-day stage, considering the different response characteristics of the device, the slow, medium, and fast subsystem layers are divided for control, and the device output related to cold, heat, electricity, and natural gas is controlled hierarchically based on distributed model predictive control. In the real-time stage, the supporting effect of IES on power grid frequency is fully explored, and an IES active-frequency-support control method considering frequency regulation cost is proposed. Case studies show that the devices can be fully utilized with different response ability to perform the scheduling plans of each layer, effectively reducing the system operation cost and improving the frequency quality.**

***Index Terms*—Integrated energy system (IES), multi-spatial-temporal-scale, optimal scheduling, model predictive control, frequency support.**

I. Introduction

As fossil fuel reserves dwindle and environmental pollution worsens, establishing a clean, efficient, and multi-energy coupling new energy system has become the key to addressing these challenges [1]. Though interacted and coupled with multiple energy sources, integrated energy system (IES) can improve energy utilization efficiency and solve energy and environmental problems [2], [3]. The dynamic characteristics of electricity, natural gas, heat, and other energy flows in IES are different. The device control characteristics and network characteristics in each energy subsystem are also different [4], coupled with the inaccuracy of the renewable energy source (RES) and load prediction, which make the scheduling of the system more difficult [5], [6]. Therefore, how to fully consider the differences in the control characteristics of each device and realize the cooperative scheduling between multiple energy systems is a critical problem that IES needs to address.

Currently, studies for coordinated optimal scheduling among multiple energy systems in IES have experienced the development from a single timescale to day-ahead-intraday multiple timescales [7], [8]. Reference [9] proposes a model predictive control (MPC)-based multi-timescale optimal scheduling method for IES considering RES uncertainties, which can improve system operation economics and accurately track stochastic fluctuations of RES. In [10], a two-stage dual-loop optimization framework for MPC-based IES is proposed to achieve coordinated operation of different energy flows on different timescales. However, the aforementioned centralized MPC method exhibits a high model order, substantial online computational demands, and poor scalability, thus making it impractical for the optimal scheduling of IES incorporating multiple distributed units. Therefore, in [11], a coordinated multi-timescale optimal scheduling method based on distributed MPC (DMPC) is presented to improve the efficiency of optimization solution for multi-microgrids. In [12] and [13], the IES energy management strategy based on DMPC is proposed to tackle the energy management under multi-timescale frameworks.

The above multi-timescale divisions are only from the perspective of improving prediction accuracy and do not consider the differences of energy response time [14], [15]. However, IES optimization, which lacks the difference in energy response time, cannot reflect the difference of control characteristics caused by the difference in response time of each energy flow, nor does it conform to the actual operation [16]. Therefore, energy response time differences must be considered in IES optimal scheduling to make the optimiza-

Manuscript received: February 10, 2025; revised: March 31, 2025; accepted: May 12, 2025. Date of CrossCheck: May 12, 2025. Date of online publication: June 5, 2025.

This work was supported by the Natural Science Research Program of Yichang City (No. A24-3-018), in part by the Hubei Provincial Natural Science Foundation Program (No. 2025AFB085), and in part by the Three Gorges University Talent Research Initiation Fund (No. Z2023404).

Y. Yang (corresponding author), P. Tang, C. Wang, N. Yang, and H. Ma are with the Hubei Provincial Key Laboratory for Operation and Control of Cascaded Hydropower Station, College of Electrical Engineering and New Energy, China Three Gorges University, Yichang, China (e-mail: epyyang@163.com; yyang_151@yeah.net; xfcancan@163.com; ynyyayy@ctgu.edu.cn; mahuizz119@126.com).

Z. Zhao is with the Department of Electrical Engineering, School of Automation, Guangdong University of Technology, Guangzhou, China (e-mail: zhuoli.zhao@gdut.edu.cn).

DOI: 10.35833/MPCE.2025.000113

tion analysis process and the final generated output plan more reasonable [17]. Hence, in [18], considering the dynamic behavior of natural gas and thermal systems, an emergency scheduling scheme based on the dynamic optimal energy flow for IES is proposed, which can reduce the energy losses during emergencies. In [19], the dynamic optimal energy flow model for IES with heat and electricity is established by combining the transient heat flow and steady-state power flow so that the system can retain the state information of the district heat network during the optimization. In [20], a day-ahead IES optimal scheduling method considering the dynamic characteristics of power-to-gas (P2G) units and natural gas pipelines is proposed to reduce the operation cost of the whole system without increasing the computational burden. Reference [21] proposes a joint optimal scheduling strategy for electricity and natural gas systems, considering the slow dynamic characteristics of natural gas pipeline networks.

In summary, existing studies have made some achievements in IES optimal scheduling, but there are still some limitations to be addressed:

1) The current research on IES multi-timescale optimal scheduling does not consider both the system prediction error and the differences in operation characteristics of multiple types of devices.

2) In IES optimal scheduling, which considers the differences in device response characteristics, the scheduling period of each device is usually fixed, i.e., it remains constant throughout the optimization process. If the scheduling period of the devices is able to adjust adaptively based on the operation conditions of the system, it will help improve the quality of system energy supply.

3) The IES supporting effect on power grid frequency is not fully explored under grid-connected operation. When the frequency changes greatly, e.g., when some nodes are connected to larger-capacity renewable energy power plants, if the supporting role of IES on frequency can be played, it will help improve the quality of power grid frequency.

To address the above limitations, this paper presents a multi-spatial-temporal-scale coordinated optimal scheduling method of IES considering the frequency support ability from both temporal and spatial perspectives, and the salient features of the proposed method are as follows.

1) Considering the device response characteristics, a multi-spatial-temporal-scale coordinated optimal scheduling framework of IES is proposed. The proposed framework enables devices with different response characteristics to reasonably perform the scheduling plans of each layer, avoids frequent adjustments to the devices, and improves the IES operation economy.

2) In the intra-day stage (IDS), an IES intra-day rolling optimization method is proposed to adaptively adjust the device scheduling period based on the errors of renewable energy and load forecasting. The method considers the smoothness of device output and prediction accuracy and improves the quality of system energy supply and system operation stability.

3) In the real-time stage (RTS), an IES frequency support control method based on virtual synchronous generator (VSG) considering the frequency regulation cost is proposed. This method makes the IES a backup of the power grid, i.e., it realizes power self-balancing in the IES with optimal operation cost when the power grid frequency remains within the acceptable range, and supports the power grid with active power when the frequency changes, which improves the power grid frequency quality.

II. Multi-spatial-temporal-scale Coordinated Optimal Scheduling Framework of IES

A. IES Structure

The structure of IES is shown in Fig. 1. The inputs are connected to the external grid and the natural gas network, and the outputs are connected to cold, thermal, electric, and natural gas loads.

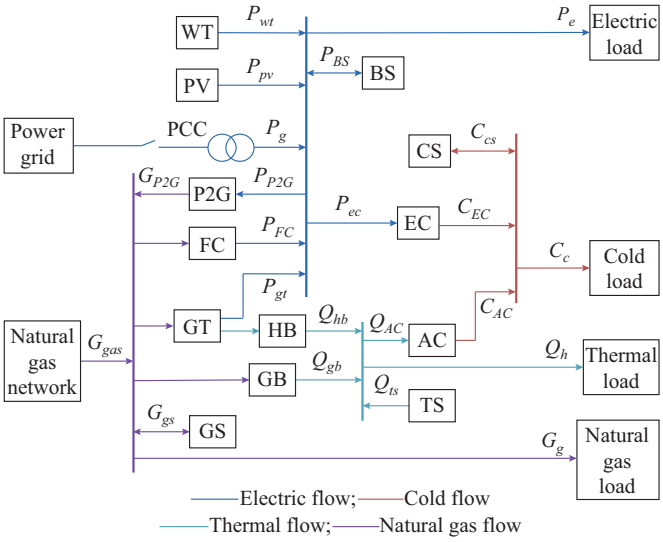

Fig. 1. Structure of IES.

The IES is composed of the energy production unit, the energy conversion unit, and the energy storage unit. The energy production unit includes photovoltaic (PV) and wind turbine (WT). The energy conversion unit includes gas turbine (GT), gas boiler (GB), waste heat boiler (HB), electric chiller (EC), absorption chiller (AC), fuel cell (FC), and P2G. The energy storage unit includes battery storage (BS) device, gas storage (GS) device, thermal storage (TS) device, and cold storage (CS) device.

B. Multi-spatial-temporal-scale Coordinated Optimal Scheduling Framework of IES

Considering the differences in the dynamic response characteristics of different energy units in the IES and the inaccuracy of RES and load forecasting, the IES optimal scheduling is classified into day-ahead stage (DAS), IDS, and RTS from the time perspective. Further consideration of the spatial scale effectively alleviates the excessive computation caused by the shortened timescale. Therefore, a multi-spatial-temporal-scale coordinated optimal scheduling framework of IES is presented, as shown in Fig. 2.

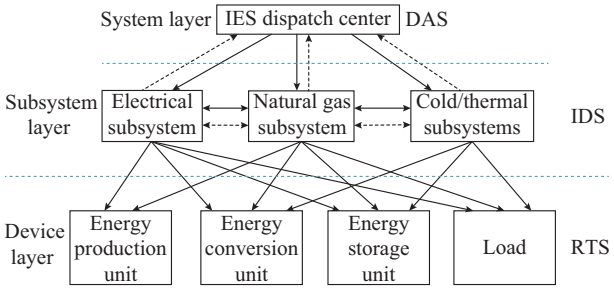

Fig. 2. Multi-spatial-temporal-scale coordinated optimal scheduling framework for IES.

Figure 2 shows that IES is divided into the system, subsystem, and device layers from the spatial scale. In this framework, the timescale of DAS is 1 hour, and the scheduling period is 24 hours, which is mainly based on the day-ahead RES and load forecasting data to formulate the day-ahead scheduling plan and provide reference information for the all-day economy operation of the system. The spatial scale uses the entire IES system.

In IDS, considering that the response speeds of electric, natural gas, and cold/thermal energy are decreasing in sequence, IDS is further divided into cold/thermal dispatch layer, natural gas dispatch layer, and electric dispatch layer. In this stage, according to the intra-day RES and load forecasting data, DMPC method is used to carry out rolling scheduling for different energy units in different timescales to achieve the objective of rolling correction of the day-ahead plan. The spatial scale uses the individual energy subsystem.

In RTS, considering that the minor changes under the system operation conditions do not affect the economy, IES is mainly used as a backup for the power grid. Power self-balancing in the IES is realized when power grid frequency remains within the acceptable range with the lowest operation cost. When the frequency changes greatly, IES responds quickly to the frequency changes to provide the necessary active support for the power grid to improve the frequency quality. The spatial scale spans the device in the electrical subsystem.

III. Optimal Scheduling Model for IES

A. DAS

1) Objective Function

In the DAS, to ensure the economic operation of IES, the day-ahead scheduling plan is developed with a timescale of 1 hour and a scheduling period of 24 hours, and the objective function is set to minimize the IES operation cost F_r as:

$$\min F_r = F_e + F_g + F_{om} \tag{1}$$

where F_e, F_g, and F_{om} are the cost of purchased electricity, the cost of purchased natural gas, and the device operation cost of IES, respectively.

1) Cost of purchased electricity

$$F_e = \sum_{t=1}^{24} (c_{b,t} P_{eb,t} - c_{s,t} P_{es,t}) \Delta t \tag{2}$$

where t indicates the time index; $c_{b,t}$ and $c_{s,t}$ are the purchased and sold prices of electricity, respectively; and $P_{eb,t}$ and $P_{es,t}$ are the purchased electricity and sold electricity, respectively.

2) Cost of purchased natural gas

$$F_g = \sum_{t=1}^{24} \left(c_{g,t} \frac{G_{gas,t}}{L_{NG}} \right) \Delta t \tag{3}$$

where $c_{g,t}$ is the natural gas price; $G_{gas,t}$ is the natural gas power purchased by IES from the gas network; and L_{NG} is the low calorific value of natural gas, with a value of 9.78 kWh/m^3 [22].

3) Device operation cost

$$\begin{cases} F_{om} = C_{gt}(P_i) + C_{bs}(P_i) + C_{fc}(P_i) \\ C_{gt}(P_i) = \sum_{t=1}^{24} (\alpha_i P_i^2 + \beta_i P_i + \gamma_i) \Delta t \end{cases} \tag{4}$$

where $C_{gt}(P_i)$, $C_{bs}(P_i)$, and $C_{fc}(P_i)$ are the operation cost functions of GT, BS, and FC, respectively; α_i, β_i, and γ_i are the corresponding cost fitting coefficients; and P_i is the output of the corresponding device.

2) Constraints

The DAS constraints include power balance constraints, operation constraints for energy conversion unit and energy storage unit, output power limit constraints for energy unit, and purchased power constraints, which are described in [22] and will not be repeated in this paper.

The day-ahead optimal scheduling model is a typical mixed-integer linear programming model. Considering that the commercial solver Cplex combines the advantages of optimization algorithms such as branch-and-bound and cut-plane, it has the ability to quickly solve mixed-integer programming problems. Therefore, this paper utilizes Cplex to solve the day-ahead optimal scheduling model.

B. IDS

Accounting for the heterogeneity in dynamic response characteristics across different energy units, if each energy unit is optimally dispatched on the same timescale, it will cause large scheduling errors. Consequently, a hierarchical scheduling architecture comprising slow, medium, and fast time scale layers is implemented in IDS to conduct multi-timescale rolling dispatch of heterogeneous energy units, thereby enabling the objective of rolling correction of the day-ahead plan. The time window for rolling scheduling is shown in Fig. 3.

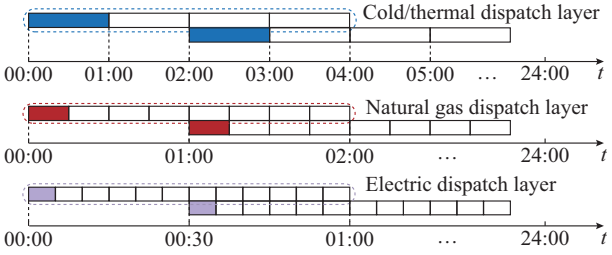

Fig. 3. Time window for rolling scheduling.

In Fig. 3, the blue dashed line is the time window (blue block) of prediction horizon, i.e., the rolling scheduling period, of the cold/thermal dispatch layer, which is 4 hours, and

the timescale is 1 hour, which is updated every 2 hours. The red dashed line is the time window (red block) prediction horizon of the natural gas dispatch layer, which is 2 hours, and the timescale is 15 min, which is updated every 1 hour. The purple dashed line is the time window (purple block) prediction horizon of the electric dispatch layer, which is 1 hour, and the timescale is 5 min, which is updated every 30 min. In this paper, considering the differences in response speeds of different devices, the timescale of BS, GT, and FC is set to be 5 min, the timescale of P2G and GS is set to be 15 min, and the timescale of GB, EC, AC, TS, and CS is set to be 1 hour.

Figure 3 shows that the corresponding cold/thermal dispatch layer is performed for 1 period, the natural gas dispatch layer is performed for 2 periods, and the electric dispatch layer is performed for 4 periods to end the first rolling schedule. At different dispatch layers, the RES output and load forecasting values on different timescales are updated. The new input values and the reference values of the day-ahead plan are used to repeat the above steps and update them in a rolling manner, thus realizing the repeated revision of the intra-day plan. MPC consists of three components: prediction model, rolling optimization, and feedback correction [23], [24], which is consistent with the rolling optimization characteristics of IDS. Through real-time feedback and rolling optimization strategies, MPC can continuously adjust the control inputs and effectively mitigate the impact of prediction error. Therefore, this paper uses MPC to solve the IDS. The basic framework of MPC is shown in Fig. 4.

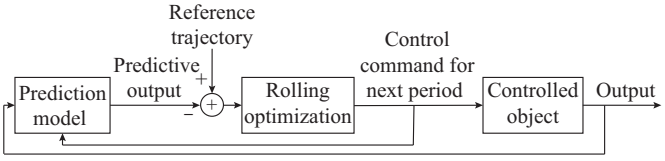

Fig. 4. Basic framework of MPC.

1) Prediction Model

MPC first needs to establish a prediction model, considering the division of IES into three subsystems: electrical, natural gas, and cold/thermal in IDS. Therefore, a DMPC method is adopted. Then, we can use the following equations to develop the prediction model for different subsystems i and j.

$$\begin{cases} \boldsymbol{x}_i(k+1)=\boldsymbol{A}_{ii}\boldsymbol{x}_i(k)+\boldsymbol{B}_{ii}\boldsymbol{u}_i(k)+\boldsymbol{E}_i\boldsymbol{d}_i(k)+ \\ \qquad\qquad \sum_{j=1,j\neq i}^{n}(\boldsymbol{A}_{ij}\boldsymbol{x}_j(k)+\boldsymbol{B}_{ij}\boldsymbol{u}_j(k)) \\ \boldsymbol{y}_i(k+1)=\boldsymbol{C}_i\boldsymbol{x}_i(k+1) \end{cases} \tag{5}$$

where $\boldsymbol{y}$, $\boldsymbol{x}$, $\boldsymbol{u}$, and $\boldsymbol{d}$ are the output, state, control, and perturbation variables, respectively; $\boldsymbol{A}_{ii}$, $\boldsymbol{B}_{ii}$, $\boldsymbol{C}_i$, and $\boldsymbol{E}_i$ are the state, control, output, and disturbance matrices of subsystem i, respectively; and $\boldsymbol{A}_{ij}$ and $\boldsymbol{B}_{ij}$ are the coupling matrices between subsystems i and j.

To obtain prediction models for each subsystem, based on the power balance equation of each subsystem and the iterative equation of the energy stored in the energy storage unit, the state of charge (SOC) of the BS serves the state variable for the electrical subsystem in (5). We select $P_{eb,t}$, $P_{es,t}$, the electric power $P_{gt,t}$ generated by GT, and the output power $P_{FC,t}$ of FC as control variables, which are also referred to as output variables. We can establish the state space equation as the prediction model for the electrical subsystem by formulating electric power $P_{ec,t}$ consumed by EC and the electric power $P_{P2G,t}$ consumed by P2G as coupling variables, along with the output electric power $P_{pv,t}$ of PV, the output electric power $P_{wt,t}$ of WT, and the electric load $P_{e,t}$ as perturbation variables.

To obtain the state space equation for electrical subsystem, the power balance equation of the electrical subsystem and the iterative equations of the energy stored in BS are first given as follows.

1) Power balance equation of electrical subsystem

$$\begin{aligned} P_{pv,t}+P_{wt,t}+P_{gt,t}+P_{eb,t}+P_{FC,t}+P_{BS,d,t}=P_{ec,t}+P_{es,t}+ \\ P_{BS,c,t}+P_{e,t}+P_{P2G,t} \end{aligned} \tag{6}$$

where $P_{BS,c,t}$ and $P_{BS,d,t}$ are the charging and discharging power of BS, respectively.

2) Iterative equations of energy stored in BS

$$\begin{cases} SOC_{t+1}=SOC_t+\left(\eta_{bs.c}P_{BS,c,t}-\dfrac{P_{BS,d,t}}{\eta_{bs.d}}\right)\Delta t \\ 0\le P_{BS,c,t}\le v_{bs,c,t}P_{BS,c,\max} \\ 0\le P_{BS,d,t}\le v_{bs,d,t}P_{BS,d,\max} \\ v_{bs,c,t}\in\{0,1\} \\ v_{bs,d,t}\in\{0,1\} \\ v_{bs,c,t}v_{bs,d,t}=0 \end{cases} \tag{7}$$

where $P_{BS,c,\max}$ and $P_{BS,d,\max}$ are the maximum charging and discharging power of the BS, respectively; $\eta_{bs,c}$ and $\eta_{bs,d}$ are the charging and discharging efficiency coefficients of the BS, respectively; $v_{bs,c,t}$ and $v_{bs,d,t}$ are the charging and discharging states of the BS, respectively; and SOC_t is the state of charge of the BS. Then, we substitute (6) into (7) to obtain state space equation for electrical subsystem as:

$$\begin{aligned} \begin{bmatrix} \dfrac{SOC_{t+1}}{\eta_{bs}} \end{bmatrix}=\begin{bmatrix} \dfrac{SOC_t}{\eta_{bs}} \end{bmatrix}+[-1,-1]\begin{bmatrix} P_{ec,t} \\ P_{P2G,t} \end{bmatrix}+[1,1,-1]\begin{bmatrix} P_{pv,t} \\ P_{wt,t} \\ P_{e,t} \end{bmatrix}+ \\ [1,-1,1,1][v_{b,t}P_{eb,t},v_{s,t}P_{es,t},P_{gt,t},P_{FC,t}]^{\mathrm{T}} \end{aligned} \tag{8}$$

where $v_{b,t}$ and $v_{s,t}$ are the power purchasing and selling states, respectively, then we have:

$$\eta_{bs}=\begin{cases} \eta_{bs,c} & v_{bs,c,t}=1 \\ \dfrac{-1}{\eta_{bs,d}} & v_{bs,d,t}=1 \end{cases} \tag{9}$$

Similarly, the predictive model can be obtained for the natural gas subsystem as:

$$\begin{cases} \begin{bmatrix} \dfrac{SOG_{t+1}}{\eta_{gs}} \end{bmatrix}=\begin{bmatrix} \dfrac{SOG_t}{\eta_{gs}} \end{bmatrix}+[1][G_{gas,t}]+[1,-1]\begin{bmatrix} G_{P2G,t} \\ G_{FC,t} \end{bmatrix}+ \\ \qquad [-1][G_{g,t}] \\ \eta_{gs}=\begin{cases} \eta_{gs,c} & v_{gs,c}=1 \\ \dfrac{-1}{\eta_{gs,d}} & v_{gs,d}=1 \end{cases} \end{cases} \tag{10}$$

where $v_{gs,c}$ and $v_{gs,d}$ are the charging and discharging states of the GS, respectively; *SOG* is the state of natural gas of the GS; η_{gs} is the efficiency coefficient of the GS; $\eta_{gs,c}$ and $\eta_{gs,d}$ are the charging and discharging efficiency coefficients of the GS, respectively; $G_{P2G,t}$ and $G_{FC,t}$ are the natural gas outputs of the P2G and FC, respectively; and $G_{g,t}$ is the natural gas load.

The prediction model can be obtained for the cold/thermal subsystem as:

$$\begin{cases} \begin{bmatrix} \dfrac{SOH_{t+1}}{\eta_{ts}} \\ \dfrac{SOI_{t+1}}{\eta_{cs}} \end{bmatrix} = \begin{bmatrix} \dfrac{SOH_{t}}{\eta_{ts}} \\ \dfrac{SOI_{t+1}}{\eta_{cs}} \end{bmatrix} + \begin{bmatrix} 1 & 0 & 0 \\ 0 & 1 & 1 \end{bmatrix} \begin{bmatrix} Q_{gb,t} \\ C_{EC,t} \\ C_{AC,t} \end{bmatrix} + \\ \qquad \begin{bmatrix} 1 & -1 \\ 0 & 0 \end{bmatrix} \begin{bmatrix} Q_{hb,t} \\ Q_{AC,t} \end{bmatrix} + \begin{bmatrix} -1 & 0 \\ 0 & -1 \end{bmatrix} \begin{bmatrix} Q_{h,t} \\ C_{c,t} \end{bmatrix} \\ \eta_{ts} = \begin{cases} \eta_{ts,c} & v_{ts,c} = 1 \\ \dfrac{-1}{\eta_{ts,d}} & v_{ts,d} = 1 \end{cases} \\ \eta_{cs} = \begin{cases} \eta_{cs,c} & v_{cs,c} = 1 \\ \dfrac{-1}{\eta_{cs,d}} & v_{cs,d} = 1 \end{cases} \end{cases} \tag{11}$$

where *SOH* and *SOI* are the states of heat and ice, respectively; $v_{ts,c}$ and $v_{cs,c}$ are the charging states of TS and CS, respectively; $v_{ts,d}$ and $v_{cs,d}$ are the discharging states of TS and CS, respectively; η_{ts} and η_{cs} are the efficiency coefficients of TS and CS, respectively; $\eta_{ts,c}$ and $\eta_{ts,d}$ are the charging and discharging efficiency coefficients of TS, respectively; $\eta_{cs,c}$ and $\eta_{cs,d}$ are the charging and discharging efficiency coefficients of CS, respectively; $Q_{gb,t}$ and $Q_{hb,t}$ are the thermal power generated by GB and HB, respectively; $Q_{AC,t}$ is the thermal power absorbed by AC; and $C_{EC,t}$ and $C_{AC,t}$ are the cold power generated by EC and AC, respectively.

2) Rolling Optimization

Since the system economy is already considered in DAS, in IDS, based on the intra-day RES and load forecasting data, the results obtained in DAS are referenced to ensure that the output of different energy units tracks the day-ahead plan as closely as possible. Therefore, the optimization objective is to minimize the adjustment amount of IES energy units, and the objective functions of each subsystem $\min\limits_{\boldsymbol{U}_{i,M}(k)} J_i(k)$ can be obtained as shown in (12). The first term in (12) is used to allow the device output to follow the reference value of DAS, and the second term in (12) is used to constrain the amplitude of the variation of the control variable.

$$\min_{\boldsymbol{U}_{i,M}(k)} J_i(k) = \left\| \boldsymbol{Y}_{i,p}(k) - \boldsymbol{Y}_{i,p}^{ref}(k) \right\|_{\boldsymbol{Q}_i}^2 + \left\| \Delta \boldsymbol{U}_{i,M}(k) \right\|_{\boldsymbol{W}_i}^2 \tag{12}$$

where $\boldsymbol{Q}_i$ and $\boldsymbol{W}_i$ are the weight coefficient matrices of the subsystem output variables and control increments, respectively; $\boldsymbol{Y}_{i,p}^{ref}(k)$ is the output reference value, i.e., the device output obtained in DAS; and $\boldsymbol{Y}_{i,p}(k)$ and $\boldsymbol{U}_{i,M}(k)$ are the predictive output variables and control sequences of subsystem i in the finite horizon at time k, respectively.

$$\begin{cases} \boldsymbol{Y}_{i,p}(k) = [\boldsymbol{y}(k+1|k), \ldots, \boldsymbol{y}(k+n|k), \ldots, \boldsymbol{y}(k+N_p|k)]^{\mathrm{T}} \\ \boldsymbol{U}_{i,M}(k) = [\boldsymbol{u}(k|k), \ldots, \boldsymbol{u}(k+n|k), \ldots, \boldsymbol{u}(k+N_c-1|k)]^{\mathrm{T}} \end{cases} \tag{13}$$

where $\boldsymbol{y}(k+N_p|k)$ is the predicted output of subsystem at k moments for the future $k+N_p$ moments; $\boldsymbol{u}(k+N_c-1|k)$ is the control sequence of subsystem at k moments for the future $k+N_c$ moments; and N_p and N_c are the prediction horizon and control horizon, respectively. $\boldsymbol{Y}_{i,p}(k)$ can be obtained by recursion from (5).

According to the established state equation prediction model of the subsystem, since there is no coupling of state variables between each subsystem, we let:

$$\begin{cases} \overline{\boldsymbol{A}_{ii}} = \begin{bmatrix} \boldsymbol{A}_{ii} \\ \boldsymbol{0} \end{bmatrix} \\ \overline{\boldsymbol{B}_{ii}} = \mathrm{diag}_{N_c}(\boldsymbol{B}_{ii}) \\ \tilde{\boldsymbol{B}}_{ij} = \sum\limits_{j=1, j\neq i}^{n} \boldsymbol{B}_{ij} \\ \overline{\boldsymbol{C}_i} = \mathrm{diag}_{N_p}(\boldsymbol{C}_i) \end{cases} \tag{14}$$

Equation (5) is written as:

$$\begin{aligned} \boldsymbol{Y}_{i,p}(k|k) = {} & \overline{\boldsymbol{C}_i}(\overline{\boldsymbol{A}_{ii}}\boldsymbol{x}_i(k|k) + \overline{\boldsymbol{B}_{ii}}\Delta \boldsymbol{U}_{i,M}(k|k) + \\ & \tilde{\boldsymbol{B}}_{ij}\Delta \boldsymbol{U}(k-1|k-1) + \boldsymbol{E}_i \boldsymbol{d}_i(k)) \end{aligned} \tag{15}$$

We let:

$$\begin{cases} \overline{\boldsymbol{C}_i}\,\overline{\boldsymbol{A}_{ii}} = \overline{\overline{\boldsymbol{A}_{ii}}} \\ \overline{\boldsymbol{C}_i}\,\overline{\boldsymbol{B}_{ii}} = \overline{\overline{\boldsymbol{B}_{ii}}} \\ \overline{\boldsymbol{C}_i}\,\tilde{\boldsymbol{B}}_{ij} = \overline{\tilde{\boldsymbol{B}}_{ij}} \end{cases} \tag{16}$$

Then, (15) can be written as:

$$\begin{aligned} \boldsymbol{Y}_{i,p}(k\,|\,k) = {} & \overline{\boldsymbol{A}_{ii}}\boldsymbol{x}_i(k|k) + \overline{\boldsymbol{B}_{ii}}\Delta \boldsymbol{U}_i(k|k) + \\ & \tilde{\boldsymbol{B}}_{ij}\Delta \boldsymbol{U}(k-1|k-1) + \overline{\boldsymbol{C}_i}\,\boldsymbol{E}_i \boldsymbol{d}_i(k) \end{aligned} \tag{17}$$

According to (17), the model predictive output of subsystem i is related to itself and the coupled subsystems.

By solving (12), the optimal solution of each subsystem can be obtained, i.e., the output of the energy unit. However, the objective functions of each subsystem in (12) only consider the optimization of respective subsystems, and the obtained solution may not be optimal. Therefore, when solving the subsystem optimization problem, it is necessary to consider both the input effect of the subsystem itself and the influence of coupling subsystems. Therefore, the improved objective function of the subsystem is:

$$\begin{aligned} \min_{\boldsymbol{U}_{i,M}(k)} J_i(k) = {} & J_i(k) + \sum_{j=1, j\neq i}^{n} J_j(k) = \left\| \boldsymbol{Y}_{i,p}(k) - \boldsymbol{Y}_{i,p}^{ref}(k) \right\|_{\boldsymbol{Q}_i}^2 + \\ & \left\| \Delta \boldsymbol{U}_{i,M}(k) \right\|_{\boldsymbol{W}_i}^2 + \sum_{j=1, j\neq i}^{n} \left[\left\| \boldsymbol{Y}_{j,p}(k) - \boldsymbol{Y}_{j,p}^{ref}(k) \right\|_{\boldsymbol{Q}_j}^2 + \left\| \Delta \boldsymbol{U}_{j,M}(k) \right\|_{\boldsymbol{W}_j}^2 \right] \end{aligned} \tag{18}$$

In (18), for subsystem i, the improved objective function includes objective function and the objective functions of the coupled subsystems, thus obtaining a globally optimal solution. In IDS, the detailed steps based on the DMPC algorithm are as follows:

Step 1: at time k, predict the initial values of each subsys-

tem. Assuming that the optimal solutions of each subsystem have been obtained at the previous moment, and each subsystem has sent its optimal solution $\boldsymbol{U}_{j,M}(k-1)$ to all other associated subsystems.

Step 2: each subsystem solves the optimal solution based on (16) and obtains the optimal solution $\boldsymbol{U}_{i,M}^{*}(k)$ for this iteration.

Step 3: according to the iterative convergence condition, if $\left|\boldsymbol{U}_{i,M}^{*(l)}(k)-\boldsymbol{U}_{i,M}^{*(l-1)}(k)\right| \le \varepsilon_n$, where ε_n is the given precision, and l is the number of iterations, then the iteration ends and goes to the next step. Otherwise, it is necessary to set $\boldsymbol{U}_{i,M}(k)= w_i\boldsymbol{U}_{i,M}^{*(l)}+(1-w_i)\boldsymbol{U}_{i,M}^{l-1}, w_i \in (0,1)$ and return to *Step 2*.

Step 4: when calculating the instantaneous control law $\Delta\boldsymbol{u}_i(k)=[1,0,\ldots,0]\boldsymbol{U}_{i,M}(k)$ for each subsystem at the current time, apply $\boldsymbol{u}_i(k)=\boldsymbol{u}_i(k-1)+\Delta\boldsymbol{u}_i(k)$ to each subsystem.

Step 5: roll to time $k+1$, then go back to *Step 1*, and the above process is repeated until the entire system optimization is completed.

2) Adaptive Adjustment of Device Scheduling Period Based on DMPC

In this paper, the scheduling period of the device is N_p in DMPC. The control performance of DMPC is dependent on N_p and N_c. In general, there is $N_c \le N_p$ for MPC. In this paper, we let $N_c = N_p$, i.e., N_c and N_p are synchronously changed. If N_p is too large, the influence of the uncertainty of the renewable energy and load forecasting on the optimal scheduling of the system will increase, and the computation time of optimization will also increase. If N_p is too small, the predictive information available for optimization may not be sufficient to fully consider the system state. Therefore, this part proposes a DMPC method that adaptively adjusts N_p based on errors of renewable energy and load forecasting. The adaptive N_p is shown in Fig. 5.

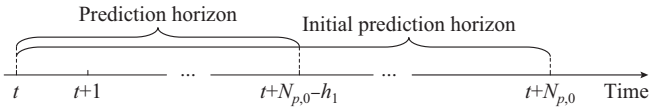

Fig. 5. Adaptive N_p.

In Fig. 5, t is the current time; $N_{p,0}$ is the initial prediction horizon step of DMPC, which is adjusted based on the sum of forecasting errors $g_{1,t}$ for RES and load; and h_1 is a piecewise function about $g_{1,t}$.

$$\begin{cases} g_{1,t} = \sum_{i=1}^{n}\left|\dfrac{P_{i,t}^{P}-P_{i,t}^{A}}{P_{i,t}^{A}}\right| \times 100\% \\ N_{p,t} = N_{p,0} - h_1(g_{1,t}) \end{cases} \tag{19}$$

$$h_1(g_{1,t}) = \begin{cases} 0 & 0 < g_{1,t} \le g_{11} \\ 1 & g_{11} < g_{1,t} \le g_{12} \\ \vdots & \vdots \\ N_{p,0}-1 & g_{1,t} > g_{1n} \end{cases} \tag{20}$$

where $P_{i,t}^{P}$ and $P_{i,t}^{A}$ are the forecasted and actual power of renewable energy and load, respectively; and $g_{11}, g_{12}, \ldots, g_{1n}$ are the intervals and $g_{1,t}$ is located, and the size of the intervals is related to the impact of $g_{1,t}$ on the optimization results. When $g_{1,t}$ has a significant impact on the optimization results, the corresponding intervals are relatively small. Otherwise, they are relatively large. The size of the intervals can be determined by selecting different N_p for multiple sets of tests under different $g_{1,t}$.

When $g_{1,t}$ is in different intervals, the value of h_1 is different. When $g_{1,t}$ is small, h_1 will decrease accordingly, and $N_{p,t}$ will increase accordingly, i.e., in the case of small $g_{1,t}$, N_p can be appropriately relaxed to consider the state of the system more comprehensively. On the contrary, N_p will be shortened to enhance prediction accuracy and optimize computation time.

C. RTS

Considering that the economy and reliability of IES operation are guaranteed in DAS and IDS, the frequency support of IES to the power grid is considered in RTS. Therefore, a frequency support method of IES based on VSG control is proposed. When the frequency changes, GT, FC, and BS with fast regulation ability are used, and the frequency regulation cost is considered to provide the necessary power support to the power grid to smooth out the frequency fluctuation. Here, VSG control is adopted in GT, FC, and BS.

1) Principle of VSG

VSG has the rotor inertia and damping characteristics of the synchronous generator (SG) by simulating the rotor operation characteristics of traditional SG. Since this paper focuses on frequency regulation, only the equation for the relationship between active power and frequency of VSG is given. The active frequency control equation of VSG can be obtained [25], [26] by referencing the SG rotor equation:

$$\begin{cases} \dfrac{\mathrm{d}\theta_m}{\mathrm{d}t} = \omega_m \\ J\omega_n \dfrac{\mathrm{d}\omega_m}{\mathrm{d}t} = P_m - P_f - D_p(\omega_m - \omega_n) \end{cases} \tag{21}$$

where J is the rotational inertia; θ_m is the rotor angle; ω_m is the rotor angle velocity; ω_n is the rated angular velocity; D_p is the virtual damping coefficient; and P_m and P_f are the mechanical power and output electric power, respectively. Based on the primary frequency regulation method of SG, P_m can be determined by the set power P_{ref} of VSG and its automatic frequency regulation output power ΔP.

$$P_m = P_{ref} + \Delta P = P_{ref} + K_p(\omega_n - \omega_m) \tag{22}$$

where K_p is the active regulation factor. According to (19) and (22), the frequency of VSG at a steady state can be obtained as:

$$\omega_m - \omega_n = \frac{P_{ref} - P_f}{K_p + D_p} \tag{23}$$

2) Optimization Model

When VSG supports power grid frequency regulation, most of the traditional methods do not consider the cost of frequency regulation, so this part proposes a VSG frequency support method that considers the cost of frequency regulation. The method optimizes the VSG power setpoint to

achieve rational active power distribution and reduce frequency regulation costs. Based on the cost function in (4), the IES optimization model for supporting grid frequency regulation can be established as:

$$\begin{cases} \min F_{om} = \sum_{i\in\{gt,bs,FC\}} C_i(P_i) \\ \text{s.t.} \sum_{i\in\{gt,bs,FC\}} \Delta P_i = \Delta P_D \quad P_{i,\min} \le P_i \le P_{i,\max} \end{cases} \tag{24}$$

where $P_{i,\min}$ and $P_{i,\max}$ are the minimum and maximum values of VSG output power, respectively; ΔP_i is the output power variation of GT, FC, and BS participating in frequency regulation; and ΔP_D is the variation of load power. Obviously, the optimal solution of the model in (24) represents the cost-optimized power setpoint for the VSG.

The Lagarange multiplier method is utilized to obtain the optimization solution of (24). Let λ represent the Lagrange multiplier corresponding to equality constraints. When inequality constraints are not considered, the optimization problem of (4) can be transformed into:

$$\min F_{om} = \sum_{i=1}^{n} C_i(P_i) + \lambda\left(\Delta P_D - \sum_{i=1}^{n} P_i\right) \tag{25}$$

By taking the partial derivative of (25), we can obtain:

$$\begin{cases} \dfrac{\partial F_{om}}{\partial P_i} = \dfrac{\partial C_i(P_i)}{\partial P_i} + \lambda = 0 \\ \dfrac{\partial F_{om}}{\partial \lambda} = \Delta P_D - \sum_{i=1}^{n} P_i = 0 \end{cases} \tag{26}$$

where $\partial C_i(P_i)/\partial P_i$ is the marginal cost of each device. According to (26), it can be obtained as:

$$\frac{\partial C_1(P_1)}{\partial P_1} = \frac{\partial C_2(P_2)}{\partial P_2} = \ldots = \frac{\partial C_i(P_i)}{\partial P_i} = -\lambda \tag{27}$$

From (27), the optimal solution of the (25) is solved when the marginal costs of the devices are consistent. In this part, the distributed consistency algorithm is introduced first and used to solve (25).

3) Solution Strategies Based on Distributed Consistency Algorithms

The first-order consistency algorithm is introduced here, whose discrete iterative equation is:

$$x_i(k+1) = \sum_{j=1}^{n} a_{ij} x_j(k) \quad i = 1, 2, ..., n \tag{28}$$

where x_i and x_j are the elements of $\boldsymbol{x}$; and a_{ij} is the weight between nodes i and j. Under the coordination of the communication network, each node exchanges information with its neighboring nodes. Driven by the distributed consensus algorithm, the discrepancy between the consensus variable values of each node and those of its neighbors continuously diminishes until consensus is achieved as:

$$x_1 = x_2 = x_3 = \ldots = x_n \tag{29}$$

Since (29) is a typical convex optimization problem, the marginal cost of each unit can be used as a consistency variable. The optimal solution of (25) can be iteratively converged through distributed consensus algorithms to obtain the optimal power setting value for VSG. The solving steps of the distributed consistency algorithm are as follows:

1) Calculate the consistency variables for each device:

$$-\lambda_i = \frac{\partial C_i(P_i)}{\partial P_i} = 2\alpha_i P_i + \beta_i \tag{30}$$

2) Based on the information at time k, update and calculate the consistency variable at time $k+1$:

$$\lambda_i(k+1) = \sum_{j=1}^{n} \alpha_{ij} \lambda_j(k) \tag{31}$$

To make the optimal power setting value of each VSG satisfy the power balance constraint in (24) after the convergence of distributed consistency iteration calculation, a feedback term is introduced into the consistency algorithm shown in (31), and the consistency variable updating formula is:

$$\begin{cases} \lambda_i(k+1) = \sum_{j=1}^{n} \alpha_{ij} \lambda_j(k) + \varepsilon \Delta f_i(k) \\ \Delta f_i(k) = f_0 - f_i(k) \end{cases} \tag{32}$$

where ε is the convergence coefficient related to the convergence speed of the distributed control algorithm; f_0 is the rated frequency; $f_i(k)$ is the measured value of the grid frequency; and $\Delta f_i(k)$ is the frequency deviation.

3) The power of the device is adjusted according to the consistency variable updated at moment $k+1$.

From (30), the output power of the device at moment $k+1$ should be updated as:

$$P_i(k+1) = \frac{-\lambda_i(k+1) - \beta_i}{2\alpha_i} \tag{33}$$

Upon each adjustment of the device power output, it is necessary to judge whether the power exceeds the limit according to inequality constraints and make corrections.

$$P_i(k+1) = \begin{cases} \dfrac{-\lambda_i(k+1)-\beta_i}{2\alpha_i} & P_{i,\min} \le \dfrac{-\lambda_i(k+1)-\beta_i}{2\alpha_i} \le P_{i,\max} \\ P_{i,\min} & \dfrac{-\lambda_i(k+1)-\beta_i}{2\alpha_i} \le P_{i,\min} \\ P_{i,\max} & \dfrac{-\lambda_i(k+1)-\beta_i}{2\alpha_i} \ge P_{i,\max} \end{cases} \tag{34}$$

From (34), to minimize the system frequency regulation cost, the marginal costs of the devices in the power range need to be consistent, while the output power of devices reaching their limits should maintain the boundary value. After several iterations, the marginal cost of each VSG converges to be consistent, i.e., the optimal power setting value of VSG is obtained.

IV. Case Studies

A. Description of Device Parameters of IES

To validate the feasibility of the proposed multi-spatial-temporal-scale coordinated optimal scheduling method, IES shown in Fig. 1 is simulated and analyzed. The parameters of each device in the IES can be found in [4]. Tables I and

II show the information of electricity and natural gas prices in IES, respectively.

TABLE I
INFORMATION OF ELECTRICITY PRICES

Period	Time interval	Electricity price (¥/kWh)
Peak	08:00-12:00 19:00-23:00	1.12
Flat	12:00-19:00	0.84
Valley	23:00-08:00	0.35

TABLE II
INFORMATION OF NATURAL GAS PRICES

Period	Time interval	Natural gas price (¥/kWh)
Peak	11:00-13:00 17:00-19:00	1.21
Flat	05:00-10:00 14:00-16:00	0.65
Valley	24:00-04:00	0.45

Figure 6 shows the power curve of RES and loads.

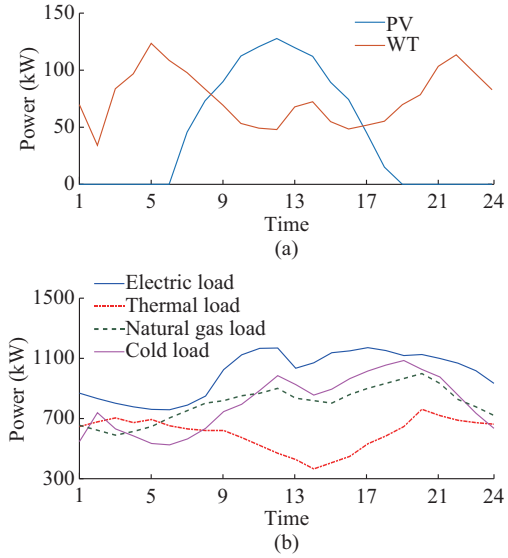

Fig. 6. Power curve of RES and loads. (a) Output power of PV and WT. (b) Load power.

B. Results and Discussion

1) Analysis of Optimization Results for DAS

Figure 7 shows the results of the day-ahead optimal scheduling, where $C_{cs,c}$ and $C_{cs,d}$ are the charging and discharging cold power generated by CS, respectively; $G_{gs,c}$ and $G_{gs,d}$ are the charging and discharging natural gas outputs generated by GS, respectively; and $Q_{ts,c}$ and $Q_{ts,d}$ are the charging and discharging thermal power generated by TS, respectively. During the low price period of electricity, IES purchases a large amount of electricity from the grid, part of which is supplied to the electric load, and the remaining electricity is stored through BS for power supply when the electricity price is high. During the low price period of natural gas, IES mainly supplies the natural gas load by purchasing the natural gas and stores the excess natural gas. The thermal load is mainly supplied by HB and GB, while the cold load is mainly supplied by EC.

During high price period of electricity, IES stops or reduces purchasing electricity from the grid, and BS starts discharging. Since the natural gas price is lower than the electricity price at this time, FC starts working, and GT assists in supplying electricity and sells the excess electricity to the grid to reduce the operation cost of the system. During high price period of natural gas, IES reduces the amount of natural gas purchased from the natural gas network. Since the electricity price is low relative to the natural gas price at this time, the natural gas load is supplied by P2G and GS discharge. When the natural gas price is high, the outputs of GB and GT will be reduced, while TS discharges heat to supply the head load, and AC supplies the cold load.

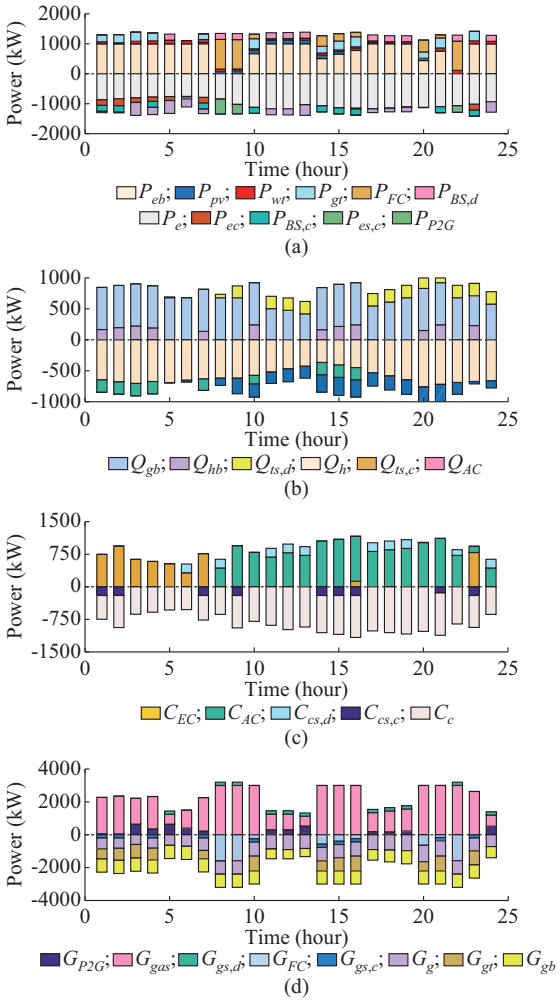

Fig. 7. Results of day-ahead optimal scheduling. (a) Electric power. (b) Thermal power. (c) Cold power. (d) Natural gas power.

During the flat price period of electricity and natural gas, IES mainly supplies electric load by purchasing electricity. Since natural gas prices are slightly lower than electricity prices, the FC output assists in supplying the electric load. Natural gas load is mainly supplied by IES through natural

gas purchased from the natural gas network, thermal load is mainly supplied by GB, and cold load is mainly supplied by AC and EC.

2) Analysis of Optimal Results for IDS

Figure 8 presents the optimal results of the cold/thermal dispatch layer in IDS.

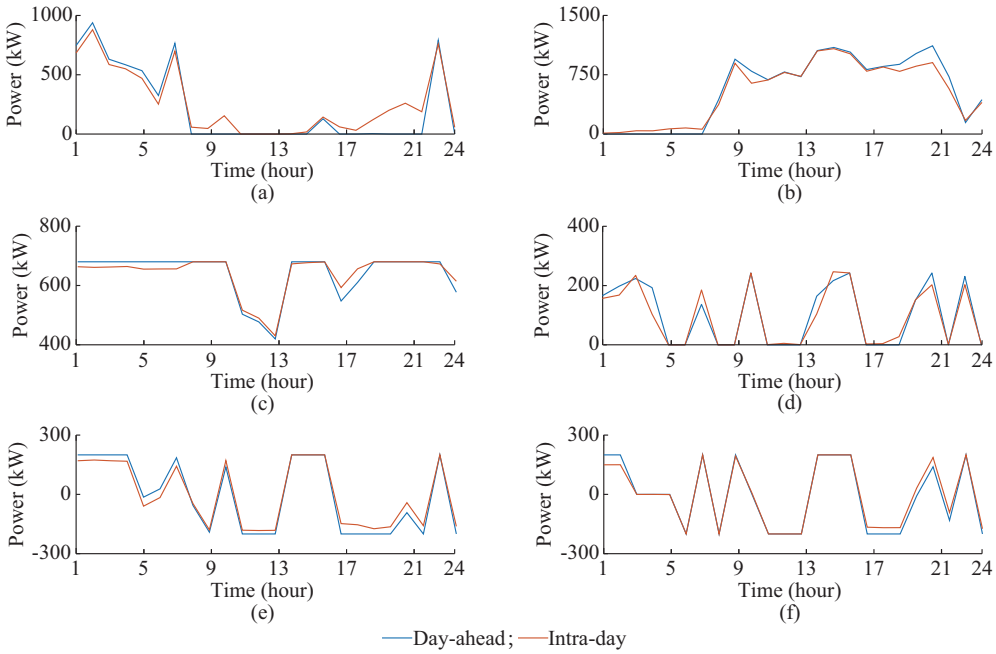

Fig. 8. Optimal results of cold/thermal dispatch layer in IDS. (a) EC. (b) AC. (c) GB. (d) HB. (e) TS. (f) CS.

At the cold/thermal dispatch layer, the output power of each energy unit is adjusted on a timescale of 1 hour. There are some differences between the output power of each device and the DAS, but the overall trend is roughly the same.

Figure 9 presents the optimal results of the natural gas dispatch layer in IDS.

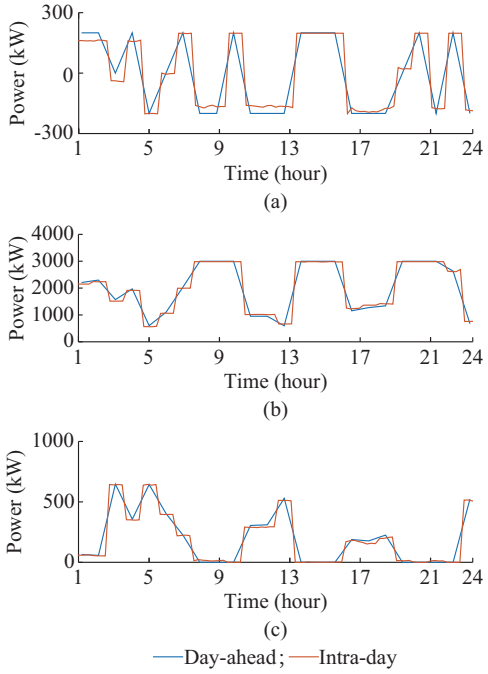

Fig. 9. Optimal results of natural gas dispatch layer in IDS. (a) GS. (b) Purchased natural gas power. (c) P2G.

At the natural gas dispatch layer, the output of each device is adjusted on a 15-min timescale. Taking G_{gas} in Fig. 9(b) as an example, IES buys a large amount of natural gas from the natural gas network to satisfy the natural gas load during the low price period of natural gas and reduces the amount of purchased natural gas during the flat price period of natural gas as well as during the peak price period of natural gas, i.e., the state of the purchased natural gas in IES accurately follows DAS. Although G_{gas} varies during different periods, the whole trend of the variation is the same. The results demonstrate that IDS effectively aligns with the scheduling outcomes of DAS, while also closely adhering to the output power requirements of the device, significantly supporting the preservation of the economic operation efficiency of the system.

Figure 10 presents the optimal results of the electric dispatch layer in IDS. At the electric dispatch layer, the output of each device is adjusted on a 5-min timescale. Taking BS in Fig. 10(a) as an example, the operation state of BS compared with DAS does not change during low price, flat price, and peak price periods, which avoids frequent switching of the operation state of BS and contributes to the prolongation of the BS lifetime. In addition, the BS output deviates from that of DAS during some periods. In IDS, the prediction accuracy of RES and loads is further improved compared with that of DAS, and the predicted power is different from that of DAS, resulting in a certain fluctuation degree of power balance, which is then required to stabilize the power fluctuation induced by BS.

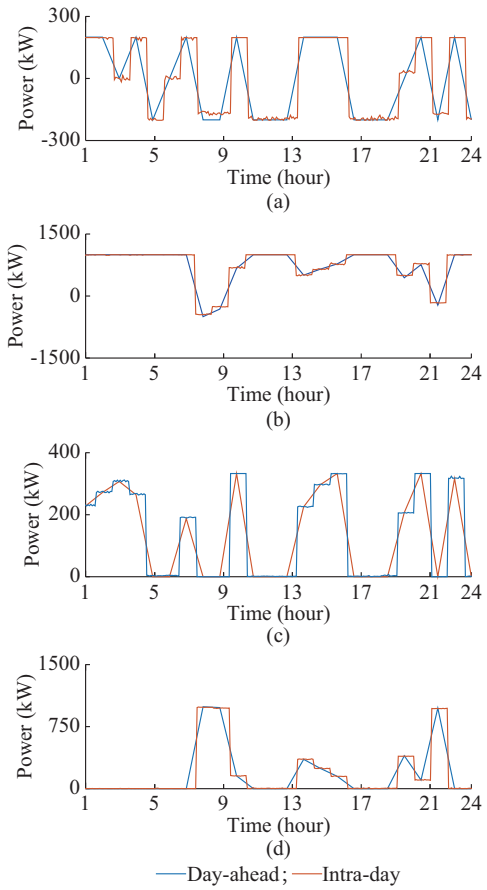

Fig. 10. Optimal results of electric dispatch layer in IDS. (a) Battery storage. (b) Purchased electric power. (c) Gas turbine. (d) Fuel cell.

3) Advantage Analysis of Proposed Multi-spatial-temporal-scale Method

To illustrate the advantages of the proposed multi-spatial-temporal-scale method, the following three cases are set up for comparative analysis. Table III shows the operation costs in three cases.

1) Case 1: set IDS timescale as 15 min.

2) Case 2: set IDS timescale as 5 min.

3) Case 3: the intra-day stage is divided into the cold/thermal, natural gas, and electric dispatch layers.

TABLE III
OPERATION COSTS IN THREE CASES

Case	Energy purchase and device operation cost (¥)	Device adjustment cost (¥)	Total operation cost (¥)
Case 1	37054	10274.0	47328.0
Case 2	40103	46847.0	86950.0
Case 3	36487	5235.8	41722.8

In DASs of cases 1-3, a 24-hour scheduling plan for the next day is formulated based on the timescale of 1 hour. Case 3 is the proposed method. Table III shows that the total operation cost of case 1 and case 2 is higher than that of case 3, which is mainly because of the increase in the number of device adjustments in IDS, i. e., the frequent adjustments of the device increase the operation and maintenance costs and the adjustment costs, thus increasing the total operation cost.

To intuitively reflect the device adjustment, the adjustment of each device in IDS is reflected by introducing the indicator of the number of device adjustments, which refers to the number of adjustments of the device relative to DAS plan during a scheduling period. The number of device adjustments in IDS is shown in Table IV.

TABLE IV
NUMBER OF DEVICE ADJUSTMENTS

Case	Number of device adjustments					
	AC	EC	GB	GS	FC	GT
Case 1	46	61	50	56	41	43
Case 2	103	115	83	123	109	98
Case 3	17	19	16	44	83	88

Table IV shows that under the single timescale operation mode of case 1 and case 2, the number of device adjustments will increase as the timescale decreases. In case 3, under the same timescale, the number of adjustments for the same device is reduced by using the multi-timescale operation method compared with the single-timescale operation method, since case 3 considers the differences in the operation characteristics of the device in the different subsystems. The hierarchical optimization of the different energy subsystems can avoid all device being optimized as variables, which reduces the number of frequent adjustments of the device. For instance, due to the slow response characteristics of AC and EC units, frequent adjustments to their outputs will not notably enhance the quality of the cold/thermal supply of the system. Instead, such adjustments will keep the system in a continuous state of transient change, thereby complicating operation optimization. Therefore, AC and EC units are not scheduled for optimization on finer timescales.

In summary, the proposed method can carry out hierarchical optimization management of device, fully considering the characteristics of device response time, so that each device can effectively perform the intra-day adjustment plan on the corresponding timescale, reduce the number of device adjustments, and then reduce the system operation costs.

4) Comparative Analysis of Adaptive N_p and Fixed N_p

To verify the superiority of the adaptive adjustment of the device scheduling period, this part first analyses the influence of the values of N_p on the optimal scheduling. Taking GB and P2G as examples, different N_p are chosen for simulation and the results obtained are presented in Fig. 11.

Figure 11(a) represents the predicted power error of GB, denoted as e_{gb}, under different N_p. The results indicate that as N_p increases, e_{gb} also increases. Figure 11(b) is the control increment of GB under different N_p, and the results indicate that the control increment of GB decreases as N_p increases, indicating that the GB output is more stable. Figure 11(c) and (d) presents the power error and control increment of P2G under different N_p, and the same conclusion can be drawn in agreement with GB, which will not be repeated here. The above results show that the values of N_p will affect the optimal scheduling of the system.

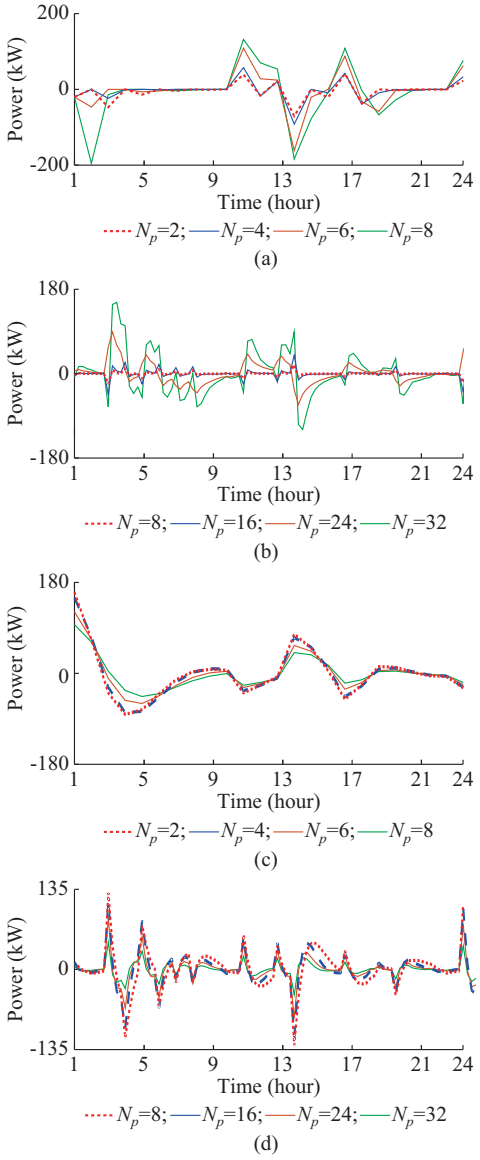

Fig. 11. Optimal results of GB and P2G under different N_p. (a) Predicted power error of GB. (b) Control increment of GB. (c) Predicted power error of P2G. (d) Control increment of P2G.

Figure 12 shows the comparison results of GB under adaptive N_p and fixed N_p. At 11:00, 14:00, and 17:00, the power error g_{res} of renewable energy and load forecasting is large.

Figure 12(a) shows that when g_{res} is large, fixed N_p makes e_{gb} larger, whereas the method of adaptive adjustment of N_p is able to adaptively adjust N_p according to g_{res}, i.e., decreases N_p in the case of large g_{res}, and thus reduces e_{gb}. Figure 12(b) shows that e_{gb} is reduced by decreasing N_p when g_{res} is large, which causes the increase of control increment of GB at that time. However, during other periods where g_{res} is small, the control increment of GB is reduced by increasing N_p, i.e., the output power of GB is smoother.

The above results show that adaptive N_p can consider both the smoothness of device output and prediction accuracy compared with fixed N_p, which improves the control performance of DMPC.

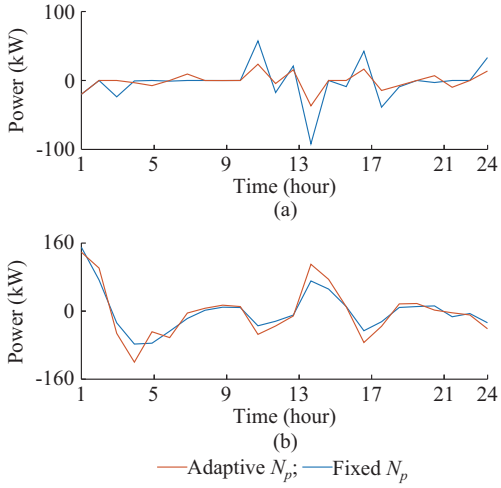

Fig. 12. Comparison results of GB under adaptive N_p and fixed N_p. (a) Predicted power error of GB. (b) Control increment of GB.

5) Analysis of Frequency Support Ability

When the power grid frequency f varies greatly, IES can respond to the frequency change and provide the necessary active support for the power grid. To verify the supporting effect of IES on f, this paper compares IES without supporting f (denoted as method 1 i.e., the benchmark), IES supporting f without considering the frequency regulation cost (denoted as method 2), and the proposed method (denoted as method 3).

Assuming that f is in the normal range at the initial time, when $t=1$ s, f drops to 0.3 Hz, and when $t=2$ s, f returns to the rated value. Figure 13(a)-(c) shows the simulation results under method 3. Figure 13 shows that at the initial time, since f is in the normal range, IES only serves as a hot standby for the power grid. Hence, the exchanged power P_g at the grid point is approximately zero, as shown in Fig. 13 (c), and the generation and consumption of power are self-balanced within IES. When $t=1$ s, f drops to 0.3 Hz, as shown by the blue line in Fig. 13(a). At this time, IES outputs 180 kW active power to the grid under the effect of frequency regulation, and f slowly drops to 49.84 Hz, as shown by the red line in Fig. 13(a). f is effectively suppressed after a short drop, indicating that IES can support f and reduce the drop of f. When $t=2$ s, f is restored, P_g is gradually restored to zero, and the output power of each unit within IES is gradually restored to the original state, as shown in Fig. 13(b). At this time, the power within IES self-balances and continues to serve as a hot standby for the power grid.

Figure 13(d)-(f) shows the simulation results under method 2, and the results show that method 2 can also support the power grid frequency. However, method 2 only considers the energy unit to share the load disturbance power according to its capacity without considering the frequency regulation cost. The increased frequency regulation cost under method 2 is calculated to be \$3619.1, while under the proposed method, the frequency regulation cost is \$3020.5, i.e., the proposed method considers the frequency regulation cost when supporting the power grid frequency, and the system economy is better.

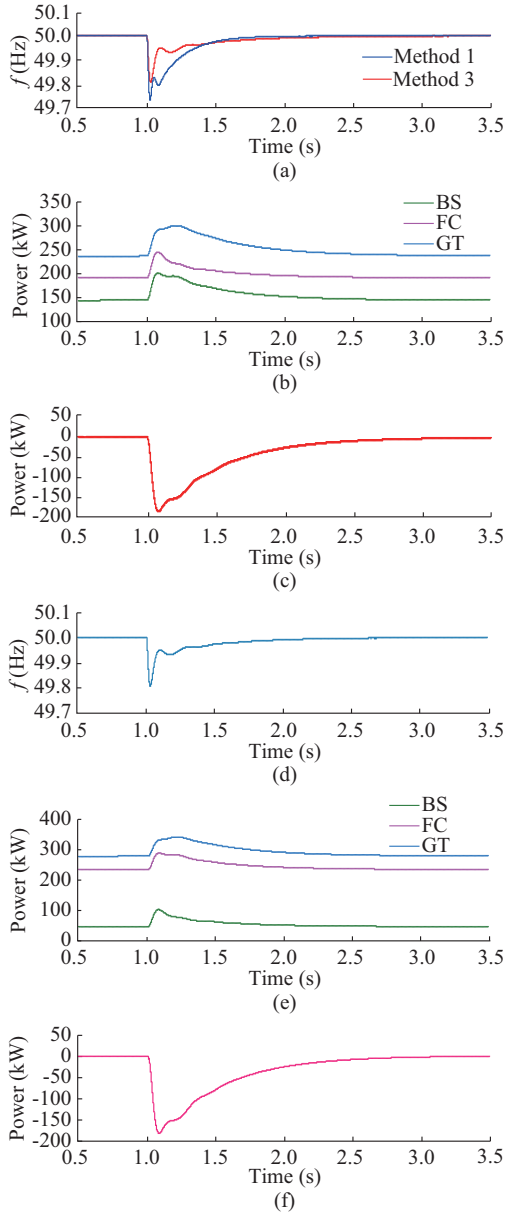

Fig. 13. Simulation results of frequency support ability. (a) System frequency under methods 1 and 3. (b) Energy unit output power under method 3. (c) Power exchange at grid-connected point under method 3. (d) System frequency under method 2. (e) Energy unit output power under method 2. (f) Exchange power at grid-connected point under method 2.

V. Conclusion

In this paper, a multi-spatial-temporal-scale coordinated optimal scheduling method of IES considering the frequency support ability is proposed, and the simulation results demonstrate the effectiveness of the proposed method. The main conclusions can be summarized as follows:

1) The proposed method considers the response time characteristics of the device so that the device with different response abilities can effectively perform the intra-day adjustment plan, which improves the IES operation economy and is more in line with the actual operation of the IES.

2) The proposed method of adaptively adjusting the scheduling period of device considers the smoothness of device output and prediction accuracy, which improves the quality of system energy supply and the stability of system operation.

3) When the power grid frequency changes greatly, the proposed method can support the frequency, reducing the drop in frequency and improving the frequency quality.

References

[1] Y. Yang, P. Zhang, C. Wang *et al.*, "State transition modeling method for optimal dispatching for integrated energy system based on cyber-physical system," *Journal of Modern Power Systems and Clean Energy*, vol. 12, no. 5, pp. 1617-1630, Sept. 2024.

[2] C. Wang, M. Wang, A. Wang *et al.*, "Multiagent deep reinforcement learning-based cooperative optimal operation with strong scalability for residential microgrid clusters," *Energy*, vol. 314, p. 134165, Jan. 2025.

[3] N. Yang, G. Xu, Z. Fei *et al.*, "two-Stage coordinated robust planning of multi-energy ship microgrids considering thermal inertia and ship navigation," *IEEE Transactions on Smart Grid*, vol. 16, no. 2, pp. 1100-1111, Mar. 2025.

[4] Y. Yang, P. Yang, Z. Zhao *et al.*, "An adaptive optimal scheduling strategy for islanded micro-energy grid considering the multiple system operating states," *IEEE Transactions on Sustainable Energy*, vol. 14, no. 1, pp. 393-408, Jan. 2023.

[5] Y. Luo, H. Yuan, Z. Hu *et al.*, "Optimal scheduling of micro-energy grid based on pareto frontier under uncertainty and pollutant emissions," *IEEE Transactions on Smart Grid*, vol. 15, no. 1, pp. 368-380, Jan. 2024.

[6] Y. Wang, J. Su, Y. Xue *et al.*, "Toward on rolling optimal dispatch strategy considering alert mechanism for antarctic electricity-hydrogen-heat integrated energy system," *IEEE Transactions on Sustainable Energy*, vol. 15, no. 4, pp. 2457-2471, Oct. 2024.

[7] L. Li, Y. Han, Q. Li *et al.*, "Multi-dimensional economy-durability optimization method for integrated energy and transportation system of net-zero energy buildings," *IEEE Transactions on Sustainable Energy*, vol. 15, no. 1, pp. 146-159, Jan. 2024.

[8] H. Li, Q. Wu, L. Yang *et al.*, "Distributionally robust negative-emission optimal energy scheduling for off-grid integrated electricity-heat microgrid," *IEEE Transactions on Sustainable Energy*, vol. 15, no. 2, pp. 803-818, Apr. 2024.

[9] Z. Zhang, C. Wang, S. Chen *et al.*, "Multitime scale co-optimized dispatch for integrated electricity and natural gas system considering bidirectional interactions and renewable uncertainties," *IEEE Transactions on Industry Applications*, vol. 58, no. 4, pp. 5317-5327, Aug. 2022.

[10] X. Dong, C. Jiang, J. Liu *et al.*, "Model predictive control optimization strategy for integrated energy systems: a two-stage dual-loop optimization framework," *IEEE Transactions on Sustainable Energy*, vol. 15, no. 4, pp. 2234-2248, Oct. 2024.

[11] Z. Zhao, J. Xu, J. Guo *et al.*, "Robust energy management for multi-microgrids based on distributed dynamic tube model predictive control," *IEEE Transactions on Smart Grid*, vol. 15, no. 1, pp. 203-217, Jan. 2024.

[12] A. Saad, T. Youssef, A. T. Elsayed *et al.*, "Data-centric hierarchical distributed model predictive control for smart grid energy management," *IEEE Transactions on Industrial Informatics*, vol. 15, no. 7, pp. 4086-4098, Jul. 2019.

[13] Y. Du, J. Wu, S. Li *et al.*, "Distributed MPC for coordinated energy efficiency utilization in microgrid systems," *IEEE Transactions on Smart Grid*, vol. 10, no. 2, pp. 1781-1790, Mar. 2019.

[14] Y. Guo, Y. Li, S. Zhou *et al.*, "Optimal dispatch for integrated energy system considering data-driven dynamic energy hubs and thermal dynamics of pipeline networks," *IEEE Transactions on Smart Grid*, vol. 15, no. 5, pp. 4537-4549, Sept. 2024.

[15] N. Yan, G. Ma, X. Li *et al.*, "Low-carbon economic dispatch method for integrated energy system considering seasonal carbon flow dynamic balance," *IEEE Transactions on Sustainable Energy*, vol. 14, no. 1, pp. 576-586, Jan. 2023.

[16] T. Wu and J. Wang, "Reliability evaluation for integrated electricity-gas systems considering hydrogen," *IEEE Transactions on Sustainable Energy*, vol. 14, no. 2, pp. 920-934, Apr. 2023.

[17] C. Zheng, J. Fang, S. Wang *et al.*, "Energy flow optimization of integrated gas and power systems in continuous time and space," *IEEE Transactions on Smart Grid*, vol. 12, no. 3, pp. 2611-2624, May 2021.

[18] M. Cao, C. Shao, B. Hu *et al.*, "Reliability assessment of integrated

energy systems considering emergency dispatch based on dynamic optimal energy flow," *IEEE Transactions on Sustainable Energy*, vol. 13, no. 1, pp. 290-301, Jan. 2022.
[19] S. Yao, W. Gu, S. Lu *et al*., "Dynamic optimal energy flow in the heat and electricity integrated energy system," *IEEE Transactions on Sustainable Energy*, vol. 12, no. 1, pp. 179-190, Jan. 2021.
[20] Z. Zhang, C. Wang, H. Lv *et al*., "Day-ahead optimal dispatch for integrated energy system considering power-to-gas and dynamic pipeline networks," *IEEE Transactions on Industry Applications*, vol. 57, no. 4, pp. 3317-3328, Aug. 2021.
[21] S. Wang, W. Wu, C. Lin *et al*., "A dynamic equivalent energy storage model of natural gas networks for joint optimal dispatch of electricity-gas systems," *IEEE Transactions on Sustainable Energy*, vol. 15, no. 1, pp. 621-632, Jan. 2024.
[22] Y. Yang, P. Yang, Z. Zhao *et al*., "A multi-timescale coordinated optimization framework for economic dispatch of micro-energy grid considering prediction error," *IEEE Transactions on Power Systems*, vol. 39, no. 2, pp. 3211-3226, Mar. 2024.
[23] P. Li, Y. Kang, T. Wang *et al*., "Disturbance prediction-based adaptive event-triggered model predictive control for perturbed nonlinear systems," *IEEE Transactions on Automatic Control*, vol. 68, no. 4, pp. 2422-2429, Apr. 2023.
[24] H. Zhang, H. Han, J. Yang *et al*., "Dynamic modeling and stability control strategy of integrated energy system in multi-time scales," *IEEE Transactions on Sustainable Energy*, vol. 15, no. 1, pp. 595-608, Jan. 2024.
[25] Z. Wang, Y. Chen, X. Li *et al*., "Impedance-based adaptively reshaping method for enhancing nonlinear load sharing and voltage quality in islanded microgrids with virtual synchronous generator," *IEEE Transactions on Smart Grid*, vol. 13, no. 4, pp. 2568-2578, Jul. 2022.
[26] Z. Wang, Y. Chen, X. Li *et al*., "Active power oscillation suppression based on decentralized transient damping control for parallel virtual synchronous generators," *IEEE Transactions on Smart Grid*, vol. 14, no. 4, pp. 2582-2592, Jul. 2023.

Yi Yang received the B.S. degree in electrical engineering from Yangtze University, Jingzhou, China, in 2015, the M.S. degree in electrical engineering from Hunan University, Changsha, China, in 2018, and the Ph.D. degree in electrical engineering from South China University of Technology, Guangzhou, China, in 2023. He is currently a Lecturer with the College of Electrical Engineering and New Energy, China Three Gorges University, Yichang, China. His research interests include power electronic for microgrid, integrated energy system optimization, and power cyber-physical system.

Ping Tang received the B.S. degree in electrical engineering from Hunan University of Technology, Zhuzhou, China, in 2024. He is currently pursuing the M.S. degree in the College of Electrical Engineering and New Energy, China Three Gorges University, Yichang, China. His research interests include integrated energy system optimization and power cyber-physical system.

Can Wang received the B.S. and M.S. degrees in control theory and engineering from Wuhan University of Science and Technology, Wuhan, China, in 2010 and 2013, respectively, and the Ph.D. degree in electrical engineering from the South China University of Technology, Guangzhou, China, in 2017. He is currently an Associate Professor of Electrical Engineering with the College of Electrical Engineering and New Energy, China Three Gorges University, Yichang, China. His current research interests include distributed generation, microgrid operation and control, integrated energy system, and smart grid.

Nan Yang received the B.S. in electrical engineering from Taiyuan University of Technology, Taiyuan, China, in 2009, and the Ph.D. degree in electrical engineering from Wuhan University, Wuhan, China, in 2014. From 2019 to 2020, he worked as a Visiting Scholar with the Stevens Institute of Technology, Hoboken, USA. He is currently a Professor at the College of Electrical Engineering and New Energy, China Three Gorges University, Yichang, China. His research interests include power dispatching automation of new energy sources, artificial intelligence, planning and operation of power systems, operation and control of microgrids, and active distribution network.

Hui Ma received the Ph.D. degree in power electronics from the School of Electric Power, South China University of Technology, Guangzhou, China. Since 2016, he has been an Associate Professor at the College of Electrical Engineering and New Energy, China Three Gorges University, Yichang, China. His current research interests include high-power density rectifier, multilevel converter, and electric energy conversion control strategy.

Zhuoli Zhao received the Ph.D. degree in electrical engineering from South China University of Technology, Guangzhou, China, in 2017. He is currently an Associate Professor with the School of Automation, Guangdong University of Technology, Guangzhou, China. His research interests include microgrid control and energy management, renewable power generation control and grid-connected operation, modeling, and analysis and control of power-electronized power systems and smart grids.